Interface-hydroxyl enabling methanol steam reforming toward CO-free hydrogen production over inverse ZrO$_2$/Cu catalyst

Xinyi Xu [a,1], Tian Lan [a,1], Guofeng Zhao [a,*], Qiang Nie [a], Fengyang Jiang [a], Yong Lu [a,b,*]

[a] Shanghai Key Laboratory of Green Chemistry and Chemical Processes, School of Chemistry and Molecular Engineering, East China Normal University, Shanghai 200062, China
[b] Institute of Eco-Chongming, Shanghai 202162, China

ABSTRACT

Methanol steam reforming (MSR), as an ideal on-site hydrogen production process, is urgently calling for a groundbreaking catalyst with ultralow or even no CO formation. Herein, we report a promising inverse ZrO$_2$/Cu catalyst system obtained by oxalate sol-gel co-precipitation and subsequent calcination/H$_2$-reduction treatment, boosting the MSR process toward CO-free hydrogen production. The preferred ZrO$_2$-0.1/Cu (Zr/Cu molar ratio of 0.1) achieves a high H$_2$ productivity of 190 mmol$_{H2}$ g$_{cat}^{-1}$ h^{-1} with undetectable CO production at 200 °C for a feed of CH$_3$OH/H$_2$O (1/1, mol/mol), while showing no deactivation throughout 200-h test by taking advantage of high sintering resistance of the inverse structure. As experimentally and theoretically unveiled, the specific ZrO (OH)-(Cu$^+$/Cu) interfacial structure is formed during the reaction, offering highly reactive interfacial -OH to convert HCHO* (formed on Cu$^+$/Cu sites from methanol; decomposable to CO/H$_2$) into H$_2$ and CO$_2$ via HCOOH* intermediate. These findings will be instrumental to tailor more-advanced MSR catalysts.

1. Introduction

Hydrogen (H$_2$) has long been deemed as an ideal multifunctional medium, able to undertake the sustainable development of future economy and society in terms of energy, environment, and chemicals [1, 2]. In particular, it offers high energy efficiency when utilized in proton exchange membrane (PEM) fuel cells that could be versatilely assembled in electric vehicles and other portable devices such as cell phones, laptop computers, etc [2]. However, the devilish problem of storing and transporting hydrogen is an obstacle for its commercial utilization in such scenarios. Methanol steam reforming (MSR: CH$_3$OH + H$_2$O = CO$_2$ + 3H$_2$) is qualified as an attractive route, by taking the advantages of high H$_2$ storage capacity of 12.5 wt% in CH$_3$OH or 12.0 wt% in CH$_3$OH/H$_2$O (1/1, mol/mol) mixture and the practicability of on-site hydrogen production under mild conditions [2–6]. Despite its rosy prospect, a groundbreaking MSR catalyst toward CO-free hydrogen production is particularly desirable to meet the requirements for example in PEMFC application (< 10 ppmv CO, a poison to anode catalyst) but remains challenging, since the methanol decomposition and reverse water gas shift reaction (forming CO) are often hard to avoid

[6].

Various supported noble/non-noble metal catalysts have been extensively explored for the MSR reaction. The noble metal catalysts (e. g., PdZn@ZnO [4], Pt/ZnO [7], and PtZn/Mo$_x$C [8]) perform with superior catalytic activity but suffer from high costs. The Ni-based ones prefer high reaction temperature and are prone to forming CO and CH$_4$ [9]. Up to date, most endeavors are focused on Cu-based catalysts (e.g., Cu/ZnO/Al$_2$O$_3$ [10], Cu/CeO$_2$ [11], Cu/Cr$_2$O$_3$ [12], Cu/MnO$_x$ [13], and Cu/ZrO$_2$ [14,15]) because of their attractive low-temperature MSR activity; most notably, the Cu/ZrO$_2$ stands out from them by virtue of its substantial potential against CO formation. For example, Ritzkopf et al. [14] prepared a nano-Cu/ZrO$_2$ catalyst by the micro-emulsion method, achieving a lower CO selectivity of below 0.1 vol% at 300 °C with a hydrogen productivity comparable to the commercial Cu/ZnO catalyst. Zhang et al. [16] modified the Cu/Al$_2$O$_3$ catalyst with ZrO$_2$ by the co-precipitation method, achieving markedly improved methanol conversion and lowered CO selectivity at 250 °C: 95% and 0.17 vol% vs. 81% and 0.37 vol% over the unmodified one. Many structural and mechanistic studies showed that the metal/oxide interface is decisive in heterogeneous catalysis [17–21], and the interface sites possess special

* Corresponding authors at: Shanghai Key Laboratory of Green Chemistry and Chemical Processes, School of Chemistry and Molecular Engineering, East China Normal University, Shanghai 200062, China
E-mail addresses: gfzhao@chem.ecnu.edu.cn (G. Zhao), ylu@chem.ecnu.edu.cn (Y. Lu).
[1] Xinyi Xu and Tian Lan contributed equally to this work.

electronic/geometric features to modulate the reaction pathways. For example, Larmier et al. [20] revealed that the Cu/ZrO_2 interface can intensify the CO_2 adsorption and thus accelerate methanol synthesis from CO_2 hydrogenation. For the MSR reaction, the Cu/ZrO_2 interface can enhance the dissociative adsorption of methanol and water to raise the catalytic performance [22]. Nevertheless, the nature of the interface sites is still insufficiently understood, and the Cu-based catalysts are plagued by the sintering of Cu nanoparticles, which both set up big obstacles for their practical applications.

In recent years, the inverse catalysts (namely loading small oxides nanoparticles onto large metal substrates to generate abundant interface sites) have received ever-increasing attentions for applications relating to heterogeneous catalysis, such as CO oxidation [23], CO_2 hydrogenation to methanol [24], and alcohol oxidation [25]. Given that the large metal substrates and oxides nanoparticles possess higher resistance to sintering than metal nanoparticles, such inverse strategy has been adopted to tailor a series of catalysts, which indeed exhibited the prolonged lifetime [25]. The inverse catalysts include not only the inverse model catalysts prepared by the precisely-controlled methods such as atomic layer deposition [24] and spraying method [26], but also the inverse catalysts prepared by the conventional simple methods such as impregnation and precipitation [27–30]. For example, Titilayo et al. used a modified co-precipitation method to generate an inverse $\alpha\text{-}Fe_2O_3/Au$ catalyst composed of 5–7 nm Fe_2O_3 particles anchored onto 15–25 nm Au particles [28]. Zeng et al. prepared an inverse CeO_2/CuO catalyst by the surfactant-templated method, with a crystallite size of 4 nm for CeO_2 and 19 nm for CuO [29]. Wu et al. synthesized an inverse 10 wt% $ZrO_2/Cu\text{-}x$ catalyst also by the co-precipitation method, and ZrO_2 (<5 nm) was supported onto the surface of Cu particles (~20 nm) [30]. For the MSR reaction, an inverse catalyst of nano-ZrO_2 supported on Cu-foil was developed, really demonstrating the promotional effect of $Cu\text{-}ZrO_2$ boundary on steering CO_2-selectivity [26]. Despite above advances, the following fundamental aspects relating to the inverse catalysts still remain ambiguous: detailed interface structure and specific interfacial active sites; mechanism of adsorption-activation of methanol and water; real pathway picture of the MSR reaction; origin of interface-enhancement effect on this reaction.

Herein, we dealt with the synthesis of an inverse ZrO_2/Cu MSR catalyst of more application potentials, being obtainable by oxalate sol-gel co-precipitation and subsequent calcination/H_2-reduction treatment. The catalyst was low-temperature active, selective and stable in the MSR reaction for a feed of CH_3OH/H_2O (1/1, mol/mol) mixture, showing a high hydrogen productivity of 190 $mmol_{H2}\ g_{cat}^{-1}\ h^{-1}$ (i.e., 4.56 $L_{H2}\ g_{cat}^{-1}\ h^{-1}$) with undetectable CO formation at 200 °C while being stable for at least 200 h. The structural and chemical origin of the highly active and selective $ZrO_2\text{-}Cu$ interface of such inverse ZrO_2/Cu catalyst was investigated by the structural and surficial probing methods (such as XPS, TEM, and probing reactions) combined with density functional theory (DFT) calculations. Both experimental and theoretical results consistently indicated the formation of specific $ZrO(OH)\text{-}(Cu^+/Cu)$ interfacial structure, which could offer highly reactive interfacial -OH that enabled the methanol-derived HCHO* species on Cu^+/Cu sites to be preferentially converted into HCOOH* intermediate (fast decomposable to CO_2/H_2) rather than to be decomposed into CO/H_2.

2. Experimental section

2.1. Catalyst preparation

The inverse $ZrO_2\text{-}x/Cu$ (x represents the Zr/Cu molar ratio) catalysts were synthesized via the oxalate sol-gel co-precipitation method. Taking the synthesis of $ZrO_2\text{-}0.1/Cu$ as an example: $Zr(NO_3)_4\cdot5H_2O$ (0.001 mol) and $Cu(NO_3)_2\cdot3H_2O$ (0.01 mol) were first dissolved into ethanol (50 mL); the ethanol solution of oxalate (0.5 M, 30 mL) was dropwise added into above nitrates solution under vigorous stirring at room temperature, and the stirring was maintained for 30 min; after aging for 2 h, the

precipitation was centrifuged and washed with ethanol for 3 times. The resultant solid was dried at 100 °C overnight, calcined in a muffle furnace at 450 °C for 3 h in air, and reduced in 10 vol% H_2/N_2 (60 mL min^{-1}) at 300 °C for 2 h to obtain the catalyst. The other catalysts of different x were synthesized by the same procedures.

2.2. Catalyst characterization

The powder X-ray diffraction (XRD) patterns were collected on a Rigaku Ultima IV diffractometer (Japan) using Cu Kα radiation at 35 kV and 25 mA, with the 2θ scanning angel of 10° to 90° and a scanning speed of 10° min^{-1}. The actual contents of Cu and Zr in catalysts were quantitatively analyzed by inductively coupled plasma-atomic emission spectroscopy on a Thermo IRIS Intrepid IIXSP ICP (USA). Transmission electron microscopy (TEM) images were obtained to visualize the morphology and nanostructure of catalysts by FEI-Tecnai G2 F30 (USA). The N_2 sorption experiments were carried out on a Quantachrome AUTOSORB-3B instrument (USA) at −196 °C to determine the specific surface area and mesoporous size distribution of catalysts, and the size distribution was obtained by the Barrett-Joyner-Halenda (BJH) method on the adsorption isotherm.

The X-ray photoelectron spectroscopy (XPS) spectra were acquired using an AXIS SUPRA system (Shimadzu/Kratos) with a standard Al Kα X-ray source (300 W) and analyzer pass energy of 30.0 eV. To avoid the contact with ambient environment, the XPS measurements were operated as follows: samples were reduced in 10 vol% H_2/N_2 (30 mL min^{-1}) at 300 °C for 2 h in the sample-pretreatment chamber (AXIS Supra, UK) and were cooled down to room temperature. Then, the samples were transferred into the XPS-measurement chamber under vacuum. All binding energies were referenced to the adventitious C1s line at 284.8 eV.

The temperature programmed desorption (TPD) experiments of different substrates (CH_3OH, H_2O) were conducted on a TP5080 multifunctional automatic adsorption instrument (Xianquan Industrial and Trading Co., Ltd., China) with a thermal conductivity detector (TCD), connected with an online mass spectrometry (MS; Proline Dycor, AMETEK Process Instrument; USA). Firstly, the catalyst (100 mg) was reduced in 10 vol% H_2/N_2 flow at 300 °C for 2 h and then cooled down to 30 °C. Later, the saturated vapor of substrate was introduced into the reactor via He-bubbling for 40 min. After purged with He for 1 h, the catalyst was heated from 30 to 700 °C in He flow, and the effluents were detected by MS spectrometer.

The CH_3OH-temperature programmed surface reaction (CH_3OH-TPSR) tests were performed on the same apparatus as TPD tests. After the same pretreatment mentioned in TPD tests, the as-treated catalyst (100 mg) was exposed to the saturated H_2O atmosphere for 40 min. Later, the reactor and catalyst therein were cleaned in He flow for 1 h at 30 °C, and the intake stream was switched to He-bubbling CH_3OH vapor. In the CH_3OH-He flow, the reactor was heated from 30 °C to the setting temperature and kept constant for 10 min. During the whole process, the as-connected MS spectrometer was used to monitor the efflux. The pulse experiments were performed on the same apparatus as above. In each test, the catalyst (100 mg) was pretreated and cooled down as mentioned in TPD tests. Afterwards, the reactor was heated to 175 °C in He flow, and each substrate (1 μL; CH_3OH, H_2O) was injected into the reactor by a microliter syringe, with the efflux recorded by the as-connected MS spectrometer online. Notably, in the TPD, CH_3OH-TPSR, and pulse experiments, the flow rates of all gases, including 10 vol% H_2/N_2 and He, were set to be 30 mL min^{-1}, and the heating rates were 10 °C min^{-1}, unless otherwise specified.

2.3. Catalyst evaluation

The MSR reaction was performed in a fixed-bed quartz tubular reactor (length of 700 mm and inner diameter of 8 mm) at atmospheric pressure. Prior to the reaction, the catalyst (0.20 g) was loaded into the

reactor and reduced in 10 vol% H_2/N_2 (60 mL min^{-1}) at 300 °C for 2 h. After reduction, the methanol-water mixture was fed into the reactor by using a peristaltic pump (Fire Track, 102 S/R, USA) at a weight hourly space velocity (WHSV) of 10 h^{-1} if not specified. The carrier gas was N_2 of 30 mL min^{-1}. The catalyst activity at each reaction temperature was analyzed after 1-h reaction to obtain the steady-state. The liquid effluent was collected by a cold trap (−5 °C) and analyzed on a Shimadzu 2014 C gas chromatography-flame ionization detector with a 30 m HP-INNOWax capillary column (DIMKA). The C-containing gas products (including CO_2, CO, CH_4) were detected on an Agilent HP 6850 gas chromatography equipped with a TCD device, which used a 30 m DM-Plot U capillary column and a 30 m DM-Plot mole sieve capillary

column in parallel. We consulted the manual of Agilent HP 6850 GC for the detection limit of TCD as < 400 pg propane/mL He (0.4 ppm). According to the measured relative correction factor of propane ($f = 0.65$) and CO ($f = 1.0$), the detection limit of CO would be less than 0.4 ppm. The methanol conversion, CO_2 selectivity, and H_2 production rate were calculated as follows:

$$\text{Conversion}_{\text{MeOH}}\ (\%) = \left(1 - \frac{n_{\text{MeOH, out}}}{n_{\text{MeOH, in}}}\right) \times 100\%$$

$$\text{Selectivity}_{\text{CO}_2}\ (\%) = \left(\frac{f_{\text{CO}_2} A_{\text{CO}_2,\ \text{out}}}{\sum f_i A_{i,\ \text{out}}}\right) \times 100\%$$

$$\text{Production Rate}_{\text{H}_2}\ (\text{mmol g}_{\text{cat}}^{-1}\ \text{h}^{-1}) = \textit{Conversion}_{\text{MeOH}} \times$$
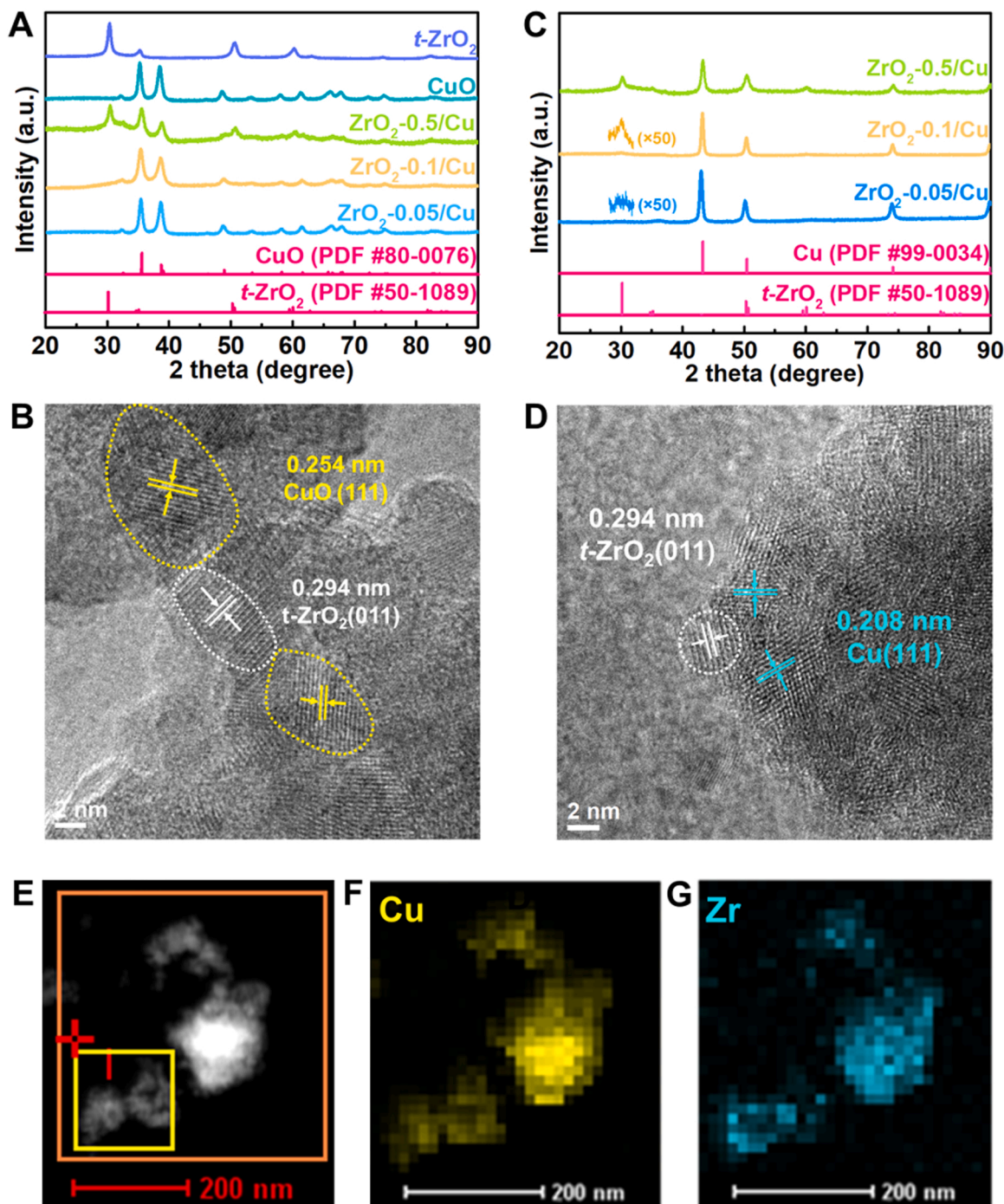

Fig. 1. Structural and nano-morphological features of fresh ZrO$_2$-*x*/CuO and reduced ZrO$_2$-*x*/Cu catalysts. (A) XRD patterns of ZrO$_2$-*x*/CuO. (B) TEM images of ZrO$_2$-0.1/CuO. (C) XRD patterns of ZrO$_2$-*x*/Cu. (D) TEM images of ZrO$_2$-0.1/Cu. (E-G) EDX mappings of ZrO$_2$-0.1/Cu.

$$\left(\frac{1}{M_{MeOH} + M_{H_2O}}\right) \times WHSV \times 3 \times 1000$$

where f_i and $A_{i,out}$ are the relative molar calibration factor and chromatographic peak area at the outlet of the individual product i (CO_2, CO, and CH_4) and f_{CO2} is the relative molar calibration factor of CO_2. The numbers of 3 and 1000 in the H_2 production rate calculation are the standard molar ratio of H_2 to CH_3OH in the MSR equation and the unit conversion (mole to millimole), respectively.

2.4. Density functional theory (DFT) calculations

The generalized gradient approximation in the Perdew-Burke-Ernzerhof (GGA-PBE function including D3 correction (Becke-Jonson damping) was employed in all density functional theory (DFT) calculations using the Vienna Ab Initio Simulation Package (VASP) code. The core valence electron interaction was described by the project-augmented wave (PAW) method, with an energy cutoff selected at 400 eV. The occupancy of the one-electron states was performed using the Gaussian smearing with SIGMA = 0.05 eV. The convergence criteria for the force and electronic self-consistent iteration were set to 0.03 eV/Å and 10^{-5} eV, respectively. The Brillouin zone integration was sampled with a grid of $3 \times 3 \times 1$ Monkhorst–Pack k-point in calculations. In order to eliminate non-local effects in transition metal systems, the DFT calculation method with the modified Hubbard U value of 4.0 eV (DFT+U) is adopted for Zr 4d electrons.

The computational model of ZrO_2/Cu were constructed with a Zr_3O_6 cluster supported by a five-Cu-layer $p(2 \times 2)$ Cu(111) slab (containing 125 Cu atoms). To avoid artificial interactions between slabs, perpendicular vacuum layers of 15 Å thick were applied in all computational models. During the optimization, the bottom three layers of bulk Cu atoms in the unit cell were frozen while the others were relaxed, including the two top layers and the Zr_3O_6 cluster.

3. Results and discussion

3.1. Structural, morphological and textural features of inverse ZrO_2/Cu catalysts

The inverse ZrO_2-x/Cu catalysts (x represents the Zr/Cu molar ratio of 0.05, 0.1, or 0.5) were synthesized by the oxalate co-precipitation method followed by calcination in air and reduction in 10 vol% H_2/N_2 flow (for details to see Method) [30]. Fig. 1A shows the X-ray diffraction (XRD) patterns of freshly calcined catalysts, as well as the ones of pure CuO and tetragonal-ZrO_2 (t-ZrO_2) as references. No ZrO_2 diffraction peaks were detected in catalysts with the Zr/Cu ratio at and below 0.1 until to a high ratio of 0.5 (t-ZrO_2 phase formed), while copper in the catalysts existed all as CuO. The average CuO crystallite size was calculated from the line-broadening width of (111) face at 2θ of 35.5° by using Scherrer equation to be 14.4 nm (ZrO_2-0.05/CuO), 11.8 nm (ZrO_2-0.1/CuO), and 10.8 nm (ZrO_2-0.5/CuO). Considering that the actual ZrO_2 contents were identical to the theoretical values (evidenced by the inductively coupled plasma-atomic emission spectroscopy examination, Table S1), the absence of ZrO_2 diffraction peaks in both ZrO_2-0.05/CuO and ZrO_2-0.1/CuO is mostly due to its high dispersion. Fig. 1B displays the transmission electron microscope (TEM) image of the typical ZrO_2-0.1/CuO catalyst, clearly observing the lattice fringes of t-ZrO_2(011) and CuO(111) with interplanar spacings of 0.294 and 0.254 nm, respectively. On the basis of above results, it was believed that ZrO_2 in the catalysts existed in its stable tetragonal structure. After reducing in 10 vol% H_2/N_2 flow at 300 °C for 2 h, strong XRD patterns of metallic Cu phase appeared in association with full obliteration of the CuO phase (Fig. 1C). The average Cu crystallite size was calculated to be 17.4 nm (ZrO_2-0.05/Cu), 15.6 nm (ZrO_2-0.1/Cu), and 14.6 nm (ZrO_2-0.5/Cu) by using Scherrer equation based on the Cu(111) XRD peak at 2θ of 43.3°. Unlike that of t-ZrO_2 XRD phase detected only in the ZrO_2-0.5/CuO, the t-ZrO_2 diffraction peaks became detectable in both

the reduced ZrO_2-0.05/Cu and ZrO_2-0.1/Cu catalysts but were very weak in comparison with that in the ZrO_2-0.5/Cu. A rational explanation is that the H_2-reduction treatment caused the aggregation of XRD-undetectable t-ZrO_2 ensembles (in freshly calcined samples; Fig. 1A) to some extent, which might be the cause for the decrease of their specific surface areas (Table S1). By calculating on the basis of Scherrer equation, the t-ZrO_2 crystalline was sized at < 2 nm (ZrO_2-0.05/Cu), 3.8 nm (ZrO_2-0.1/Cu), and 14.9 nm (ZrO_2-0.5/Cu), for example, only a fourth of that (15.6 nm) of Cu grain in case of the ZrO_2-0.1/Cu; this suggested the existence of inverse t-ZrO_2/Cu structure. As can be seen from the TEM images (Fig. 1D) and energy dispersive spectroscopy (EDS) elemental mappings (Fig. 1E-G), indeed, the representative ZrO_2-0.1/Cu catalyst showed clear inverse t-ZrO_2/Cu contacting structure (typically, the t-ZrO_2 nano-fragments of 3–4 nm were highly dispersed onto the large Cu particles of ~20 nm with their distinct interlaced lattice fringes of t-ZrO_2(011) and Cu(111)).

The evolution of surface chemical states transferring from the fresh ZrO_2-0.1/CuO to the reduced ZrO_2-0.1/Cu was also monitored by XPS, with the results shown in Fig. S1. On the fresh catalyst surface, only Cu^{2+} species in CuO was detected, solidly evidenced by the Cu $2p_{3/2}$ and Cu $2p_{1/2}$ peaks at 934.2 and 954.0 eV together with the shake-up satellite peaks at 943.1 and 962.5 eV accordingly [31]. On the reduced catalyst surface, the shake-up satellite peaks disappeared while the full widths at half maximum peaks of Cu $2p_{3/2}$ and Cu $2p_{1/2}$ became narrower and shifted to lower binding energies, indicating the complete reduction of CuO. Moreover, Auger electron spectrum, acquired for the reduced ZrO_2-0.1/Cu in the kinetic region of 905–926 eV, indicated the thorough transformation of CuO into Cu^0 by ruling out the existence of Cu^+ species (Fig. S1). In the course of CuO-to-Cu^0 evolution, no shift of the Zr 3d binding energy was observed, showing that t-ZrO_2 held its chemical state unchanged. It is thus safe to say that a (Cu^{2+}/Cu^+)-contaminant-free t-ZrO_2-Cu interface could be achieved on our inverse t-ZrO_2/Cu catalysts.

3.2. Catalytic performance of the inverse ZrO_2/Cu catalysts

The MSR performance of the reduced ZrO_2-x/Cu ($x = 0.05$, 0.1, or 0.5) catalysts was evaluated at 200–300 °C and atmospheric pressure, using a feed of CH_3OH/H_2O (1/1, mol/mol) mixture with a weight hourly space velocity (WHSV) of 10 h^{-1}. Along with the rise of Zr/Cu molar ratio from 0.05 to 0.5, the methanol conversion and H_2 production rate exhibited a volcano-like evolution at each reaction temperature (Fig. 2A). For instance, at 200 °C, the ZrO_2-0.1/Cu achieved a high H_2 productivity of 190 $mmol_{H2}$ g_{cat}^{-1} h^{-1}, 2.1 or 1.7 times higher than that of the ZrO_2-0.05/Cu (93 $mmol_{H2}$ g_{cat}^{-1} h^{-1}) or the ZrO_2-0.5/Cu (115 $mmol_{H2}$ g_{cat}^{-1} h^{-1}). Most notably, the undesired byproducts of CO and CH_4 were undetectable for all catalysts at 200 °C, regardless of varying the WHSV from 5 to 20 h^{-1} and the H_2O/CH_3OH molar ratio from 0.5/1 to 3/1 (Fig. S2). Fig. 2A, B also shows the strong temperature dependence of methanol conversion, H_2 productivity, and CO_2 selectivity for all three catalysts. When increasing the temperature from 200 to 300 °C, the methanol conversion and H_2 productivity were markedly enhanced, for example, by a factor of 1.7 for the ZrO_2-0.1/Cu, whereas the CO_2 selectivity showed an opposite trend (decreased from 100% at 200 °C to, for example, 96.5% at 300 °C for the ZrO_2-0.1/Cu).

The durability of MSR catalysts is of utmost importance; however, the traditional Cu-based ones often suffer from rapid deactivation due to the severe nano-Cu sintering. The stability of our inverse ZrO_2/Cu catalysts was checked by adopting the ZrO_2-0.1/Cu in 200-h MSR reaction test at 200 °C, using the CH_3OH/H_2O (1/1, mol/mol) feed with a WHSV of 10 h^{-1}. In Fig. 2C, the H_2 production rate and CO_2 selectivity are plotted against the time on stream, showing a good H_2 productivity maintenance (180–200 $mmol_{H2}$ g_{cat}^{-1} h^{-1}) with no detectable CO formation (i.e., 100% CO_2 selectivity) throughout entire test. It is believed that the high catalytic stability profits from the inverse ZrO_2/Cu structure of such catalyst, because of the outstanding anti-sintering ability of
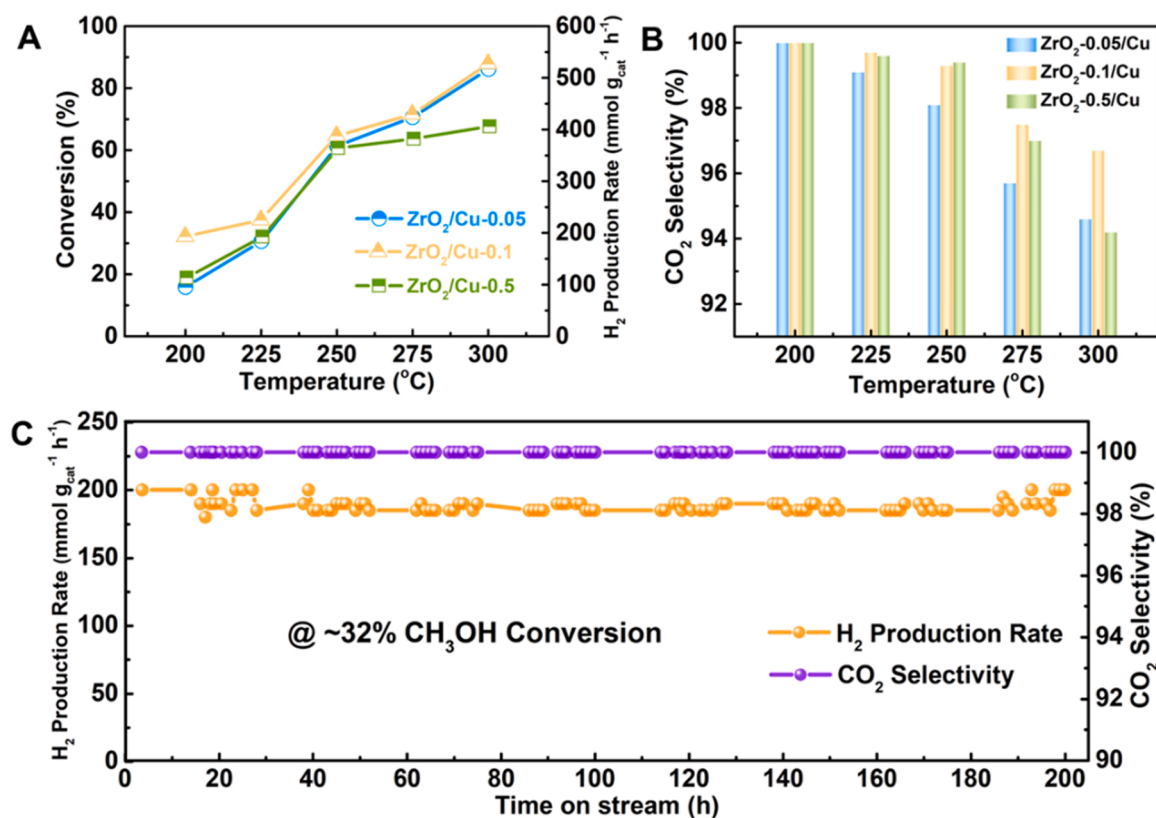
Fig. 2. MSR results of ZrO$_2$-*x*/Cu catalysts. (A) methanol conversion, H$_2$ production rate and (B) CO$_2$ selectivity of the ZrO$_2$-*x*/Cu catalysts. (C) H$_2$ production rate and CO$_2$ selectivity against time on stream over the ZrO$_2$-0.1/Cu at 200 °C. Other reaction conditions: total WHSV of 10 h^{-1}, CH$_3$OH/H$_2$O molar ratio of 1.0, and 0.1 MPa.

both large Cu particles (~16 nm; T$_{Tammann}$ of 427 °C, T$_{Hüttig}$ of 171 °C) and nano-ZrO$_2$ fragments (~4 nm; T$_{Tammann}$ of 1218 °C, T$_{Hüttig}$ of 673 °C) compared to the small Cu nanoparticles (e.g., 3–4 nm; T$_{Tammann}$ of 299 °C, T$_{Hüttig}$ of 90 °C) [32–34]. Particularly, the high-purity H$_2$ with undetectable CO (i.e., CO-free H$_2$) is attractive for an on-site compact H$_2$ fuel supplier in PEMFC applications, because of no need of the downstream multistage CO post-treatments. For comparison, the MSR reaction results over our inverse ZrO$_2$-0.1/Cu and other typical reported catalysts are summarized in Table S2. Clearly, our catalyst is comprehensively superior over the literature catalysts with respect of the H$_2$ productivity, long-term stability, and especially the CO-free H$_2$ production ability.

It should be pointed out that the CO-free hydrogen production at a high rate of 190 mmol$_{H2}$ g$_{cat}^{-1}$ h^{-1} was achieved at 200 °C with a CH$_3$OH conversion of ~32% using a WHSV of 10 h^{-1}. Nevertheless, low conversion seems not a gross defect because the unreacted CH$_3$OH/H$_2$O mixture (with unchanged molar ratio of 1/1, due to no occurrence of side reactions such as CH$_3$OH decomposition) can be easily collected and stored in feed tank for use again. Of course, a high conversion (95.6%) could be achieved over ZrO$_2$-0.1/Cu at 200 °C by using an unacceptably low WHSV of 0.25 h^{-1}; not surprisingly, a low CO-free H$_2$ productivity of only 14 mmol$_{H2}$ g$_{cat}^{-1}$ h^{-1} could be obtained (Table S3).

3.3. Activity and selectivity origin from the t-ZrO$_2$-Cu interface

As can be seen in Fig. 2A, the H$_2$ production rate was doubled from 93 to 190 mmol$_{H2}$ g$_{cat}^{-1}$ h^{-1} with rising the Zr/Cu molar ratio from 0.05 to 0.1 (corresponding to ZrO$_2$ content from 9 to 18 wt%) at 200 °C, preliminarily indicating that the MSR performance of our inverse ZrO$_2$/Cu catalysts was linked with their ZrO$_2$-Cu contacting interface. Two single-component catalysts of pure Cu substrate and *t*-ZrO$_2$ were also tested under the identical reaction conditions and both showed very poor

activity (especially in case of *t*-ZrO$_2$, no CH$_3$OH conversion detected; Table S4), in turn firmly confirming that the ZrO$_2$-Cu interface (rather than the individual ZrO$_2$ or Cu component) was highly active for the MSR reaction. Aiming to this deduction, a series of contrastive ZrO$_2$/Cu catalysts were prepared by using low ZrO$_2$ contents from 2 to 9 wt% (corresponding to Zr/Cu molar ratio from 0.01 to 0.05) for ensuring the linear increase in the ZrO$_2$-Cu interface quantity with ZrO$_2$ content and tested in the MSR reaction under identical reaction conditions. As expected, the H$_2$ production rate presented a linear increase with rising the ZrO$_2$ content from 2 to 9 wt% but a reversed trend with rising the Cu content (Fig. S3). In addition, the poor MSR activity of pure *t*-ZrO$_2$ (Table S4) also rules out the possibility that the ZrO$_2$ sites were responsible for the linearly-increased activity. These results lock the ZrO$_2$-Cu interface catalysis in this reaction. Furthermore, the apparent activation energies (E$_a$) of ZrO$_2$-0.1/Cu, pure Cu, and *t*-ZrO$_2$ were gained to probe the intrinsic activity of their corresponding active sites. As depicted in Fig. S4, the ZrO$_2$-0.1/Cu achieved the lowest E$_a$ of 61 kJ mol^{-1}, 1 or 2 times lower than that of the pure Cu (147 kJ mol^{-1}) or *t*-ZrO$_2$ (186 kJ mol^{-1}). These contrastive and kinetic results consistently consolidate that the ZrO$_2$-Cu interface was the origin of the substantially enhanced activity of our inverse ZrO$_2$/Cu catalysts.

In order to unveil the ZrO$_2$-Cu interface structure, the ZrO$_2$-0.1/Cu catalyst after the MSR reaction at 200 °C was initially probed by XRD and TEM/EDS, showing the diffraction peaks of Cu and *t*-ZrO$_2$ (Fig. 3A, with intensity and width comparable to those of the reduced one in Fig. 1C) and the well-preserved nanomorphology (i.e., the *t*-ZrO$_2$ nanofragments mounted on the large Cu particle, Fig. 3B-E, Fig. S6). Unlike the reduced one (Fig. 1C), the formation of some Cu$_2$O was clearly detected by XRD (Fig. 3A), which was widely reported to be originated from H$_2$O-oxidation [35]. Besides this remarkable change, a clear evolution of the chemical and electronic states of Zr element on the used ZrO$_2$-0.1/Cu catalyst surface was monitored by the surface-sensitive
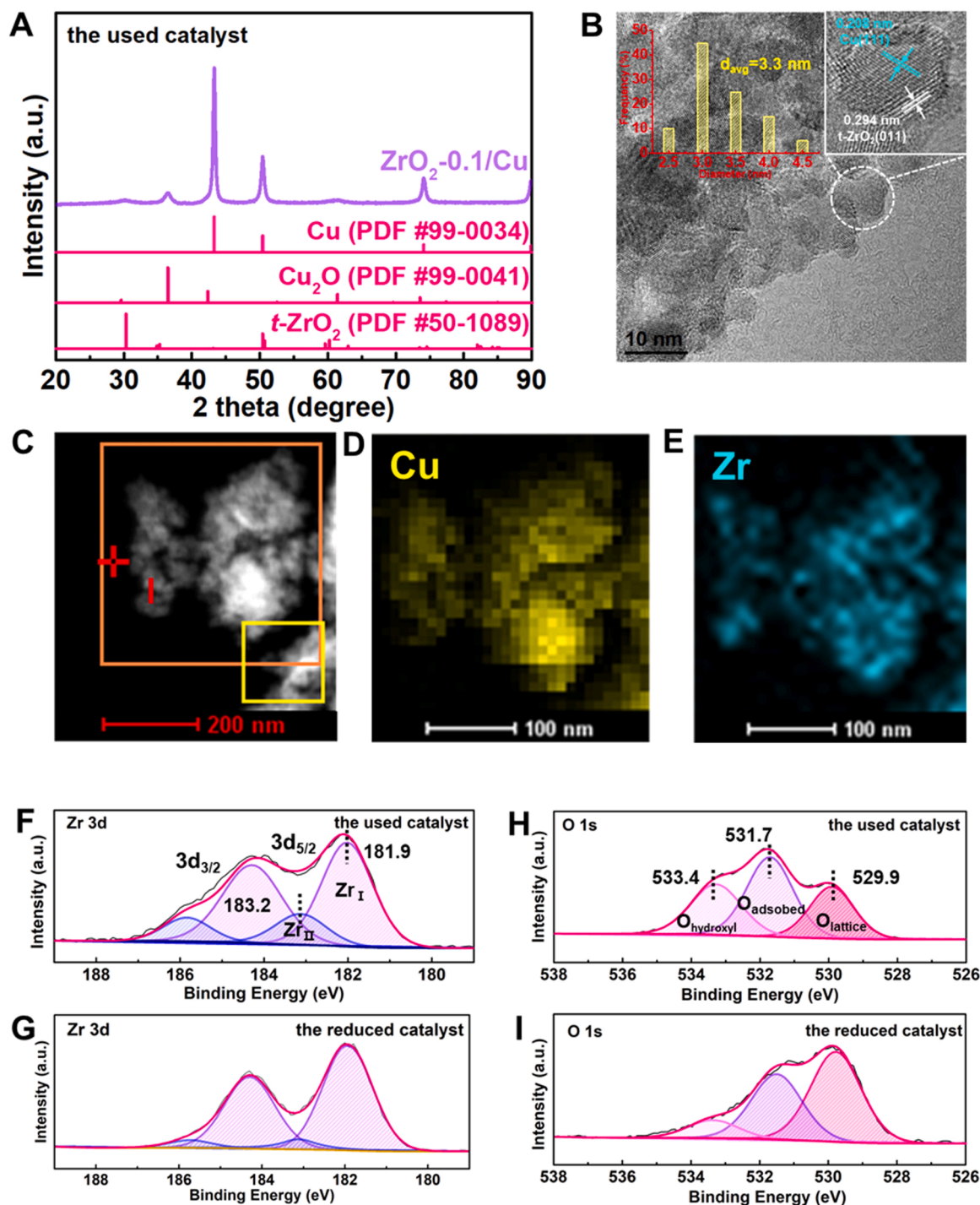
Fig. 3. Structural, nano-morphological, and surface chemical features of reduced and used ZrO_2-0.1/Cu catalysts. (A) XRD patterns, (B) TEM images (insets: corresponding size distribution of the *t*-ZrO_2 nanoparticles, see also Fig S6), (C-E) EDS mappings of used ZrO_2-0.1/Cu catalyst, (F, G) XPS spectra of Zr 3d for (F) used and (G) reduced ZrO_2-0.1/Cu catalyst, (H, I) XPS spectra of O 1 s for (H) used and (I) reduced ZrO_2-0.1/Cu catalyst.

XPS. It is clear from the Zr 3d region XPS spectrum in Fig. 3F that there were two kinds of Zr species on such used catalyst surface: species I (Zr_I) with a low binding energy (B.E.) at 181.9 eV, and species II (Zr_{II}) with a high B.E. at 183.2 eV. The Zr_I was assignable to pure ZrO_2, while the Zr_{II} is to Zr-OH according to the report by Sato et al. [36]. Most notably, the molar fraction of surface Zr-OH in the total surface Zr species is raised from 8% for the reduced catalyst to 28% for the used one (Fig. 3F, G and Table S5). Such newly formed Zr-OH species could be further evidenced by the O 1s region XPS spectrum (detailed results and discussion to see Fig. 3H, I and Table S5), which is attributed to the H_2O decomposition at

the ZrO_2-Cu boundary [22]. On the basis of above results, we are confident that the original *t*-ZrO_2-Cu interface for freshly reduced ZrO_2-0.1/Cu catalyst is evolved into the $ZrO(OH)$-(Cu^+/Cu) complex interface on stream, which imparts the catalyst with high activity and selectivity for the MSR reaction.

3.4. The role of Cu and t-ZrO₂ in synergistic catalysis

3.4.1. Insight into the role of Cu⁺/Cu sites

In order to gain the insight into catalysis mechanism at the ZrO_2-Cu

interface, the adsorption and activation of CH$_3$OH and H$_2$O was first studied on the individual surface of Cu or t-ZrO$_2$ by the temperature-programmed techniques. Considering that the Cu species in used catalyst exists mainly in the metallic form, the CH$_3$OH-temperature programmed desorption (TPD) experiments were initially performed on pure Cu^0 substrate. No clear desorption of CH$_3$OH or other species emerges from 30 to 700 °C (Fig. 4A), indicating negligible CH$_3$OH adsorption on metallic Cu^0 sites, which is in line with other reported results that the neat Cu surface just applied a weak CH$_3$OH adsorption [37]. The CH$_3$OH-temperature programmed surface reaction (TPSR) was then conducted on this sample, with results shown in Fig. 4B. As we can see, very weak mass spectrum (MS) signals for HCHO, CO, and H$_2$ were detected even at 250 °C, while showing complementary evolution between CO/H$_2$ and HCHO. It is thus believed that the pure Cu^0 substrate (i.e., ~20 nm Cu^0 particles similar to the counterparts in our ZrO$_2$/Cu inverse catalysts) is poorly active for CH$_3$OH decomposition to CO/H$_2$ via HCHO intermediate. In addition, since some Cu$_2$O exists in the used catalyst (Fig. 3A), CH$_3$OH-TPD was also done over a pure Cu$_2$O compound, showing that the deep oxidation of pre-adsorbed CH$_3$OH took place other than its desorption, decomposition (to form CO/H$_2$), and/or partial oxidation (to form HCHO), evidenced by the formation of CO$_2$ as only carbon-containing product (peaked at 375 °C, Fig. 4C; H$_2$O was not detected). According to such distinct CO$_2$ MS signals, moreover, it is rational to infer that CH$_3$OH would be adsorbed on Cu$_2$O more easily and strongly than on Cu^0.

Since H$_2$O is a reactant in the MSR reaction, it is necessary to understand whether and how it would modulate the CH$_3$OH activation on Cu^0 surface. To gain this goal, H$_2$O was first adsorbed on the pure Cu^0 substrate at 200 °C. Eren et al. [38] reported the co-existence of Cu^0,

Cu$^+$, and OH groups on Cu foil after exposed in H$_2$O vapor. Indeed, the Cu^0 substrate was partially oxidized into Cu$_2$O/Cu after H$_2$O-adsorption at 200 °C (evidenced by a clear Cu$_2$O XRD phase (Fig. S5A) with the peak intensity comparable to that for the used ZrO$_2$-0.1/Cu as shown in Fig. 3A), with existence of some surface OH species (evidenced by the IR bands at 3460, 1636, 1386 cm^{-1}, Fig. S6B). After that, the CH$_3$OH-TPSR was performed on this sample. As we can see in Fig. 4D, the HCHO started to be formed at 30 °C and continuously increased with temperature rising to 150 °C, while holding almost unchanged until next temperature rose up to 175 °C; meanwhile, the H$_2$ formation was not detectable below 150 °C. A reasonable explanation is that the CH$_3$OH dehydrogenation was very easy on the co-existing Cu^0/Cu$^+$ sites to HCHO (adsorbed on Cu$^+$, [35] easily desorbed from 30 °C) and H (on Cu^0, [39] recombining to be desorbed as H$_2$ from 150 °C). The MS signal of HCHO immediately showed a little steep drop in association with the transient formation of a relatively large amount of CO$_2$/H$_2$ but a small amount of CO, while HCOOH formation was also detected in trace amount, only when temperature rising up to 175 °C (Fig. 4D). Actually, for the Cu-catalyzed MSR reaction, it was well proven that HCHO intermediates from CH$_3$OH could efficiently react with Cu-OH to form HCOOH, which could decompose rapidly on Cu-sites into CO$_2$/H$_2$ [15, 40].

By combining above present-results with the reported-studies, the following conclusions can be drawn: the co-existing Cu^0/Cu$^+$ sites enable the dissociative CH$_3$OH adsorption to HCHO (on Cu$^+$) and H (on Cu^0); Cu-OH facilitates the conversion of HCHO into HCOOH, followed by HCOOH decomposition into CO$_2$/H$_2$ at low temperature. This is why only CO/H$_2$ formation was detected in the CH$_3$OH-TPSR profiles over the Cu^0 substrate (Fig. 4B), but dominant CO$_2$/H$_2$ over the Cu^0 substrate
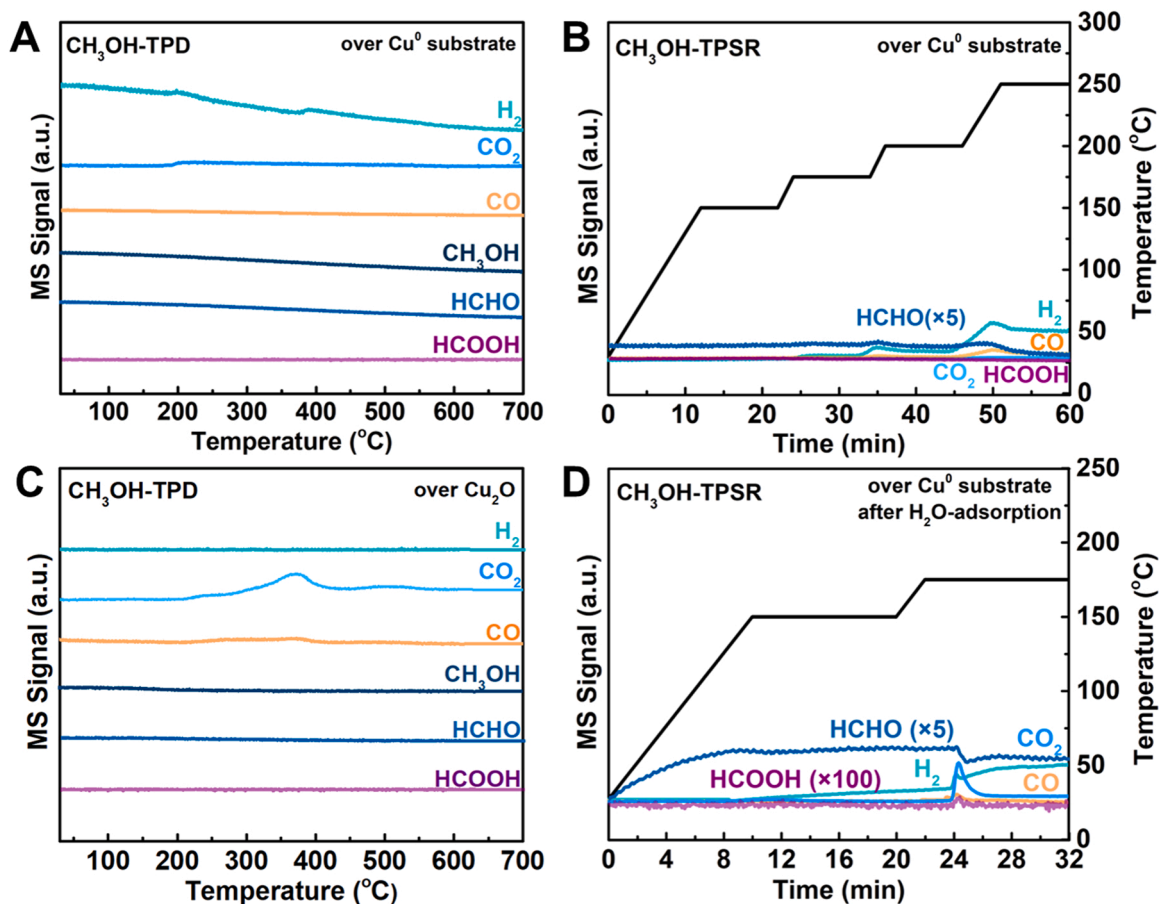

Fig. 4. (A, C) CH$_3$OH-TPD and (B, D) CH$_3$OH-TPSR profiles. Samples: in (A) and (B), pure Cu^0 substrate; in (C), Cu$_2$O; in (D), pure Cu^0 substrate after H$_2$O adsorption at 200 °C.

after pre-adsorption of H_2O (Fig. 4D). However, the inadequate capacity for activating H_2O on Cu surface results in the limited OH groups thereon [41], thus obstructing the sufficient HCHO transformation into HCOOH and finally into CO_2/H_2. It is not surprising that only small amount of CO_2/H_2 was detected due to the rapid consumption of very insufficient -OH groups on Cu substrate. We thus believe that the Cu^0/Cu^+ sites are mostly responsible for the adsorption and activation of CH_3OH to offer the HCHO species.

3.4.2. Insight into the role of t-ZrO₂ sites

The CH_3OH-TPD was conducted over the pure t-ZrO_2 that was pre-treated at 500 °C in He flow to clean its surface [42]. The profiles in Fig. 5A show that the desorption of CO and H_2 occurred and peaked at around 400 °C, while trace HCHO and CH_3OH were always detected from 70 to 550 °C (then nothing left behind). A very weak MS signal of HCOOH was also detected at 350 °C but no CO_2 was formed. The above results indicated the effective adsorption of CH_3OH on t-ZrO_2 surface and its further conversion into CO/H_2 (dominant) as well as HCHO (trace) and HCOOH (trace); and notably, there seems no association between HCHO formation and the formation of H_2/CO even HCOOH. Then, the H_2O-TPD was carried out, showing three H_2O-desorption peaks at 110, 200 and 500 °C (Fig. S7A). In general, the ZrO_2 surface is easily covered by adsorbed water and -OH groups while removing -OH requires a high temperature around 500 °C [43,44]. Accordingly, the two peaks at 110 and 200 °C are ascribed to the weakly-adsorbed water and the peak at 500 °C is classified as the recombination of surface -OH groups ($2Zr-OH \rightarrow Zr-O + H_2O$). Clearly, the dissociative adsorption of H_2O is more favorable on the t-ZrO_2 surface, in comparison with the Cu^0 substrate (Fig. S7B).

To probe the reactivity of -OH groups on t-ZrO_2 surface with CH_3OH, the CH_3OH-TPSR was then performed on the t-ZrO_2 that was exposed in H_2O-vapor at 200 °C and subsequently flushed in He flow at 300 °C for 0.5 h (to remove physically adsorbed water). In the profiles shown in Fig. 5B, the HCHO formation was always detected until to 400 °C but showed a downward trend with rising temperature; sufficient formation of HCOOH started at 150 °C while showing a trend opposite to the HCHO formation with rising temperature up to 400 °C. This observation indicated that -OH groups on t-ZrO_2 surface not only promoted the CH_3OH dehydrogenation to form HCHO (compared to the MS signal intensity on the OH-free t-ZrO_2; Fig. 5A), but also were highly active to react with HCHO to form HCOOH (the HCHO-TPSR over this t-ZrO_2 sample was performed, also yielding HCOOH dominantly (not shown)). Moreover, very small amounts of $CO/CO_2/H_2$ were formed even at 400 °C, implying that the Cu-free t-ZrO_2 surface even with -OH groups is almost inert for the catalytic decomposition of CH_3OH, HCHO, and/or HCOOH below 400 °C. Only when further rising temperature from 400 up to 500 °C, the CO/H_2 formation was detected in large amount but CO_2 in trace amount, while the signal of HCHO/HCOOH showed a rapid decrease until complete disappearance. A possible explanation is that the direct CH_3OH decomposition and/or its indirect decomposition via HCHO to form CO/H_2 became dominant above 400 °C over t-ZrO_2.

3.4.3. Synergistic catalysis at t-ZrO₂-Cu interface

Our ZrO_2/Cu catalysts outperform the individual counterpart of either pure Cu substrate or t-ZrO_2 (Table S4). By combining this fact with the findings that neither Cu^+/Cu sites on Cu substrate nor -OH groups on t-ZrO_2 are working individually with efficient MSR performance (Fig. 4D and Fig. 5A, B), we are thus more confident that there should exist
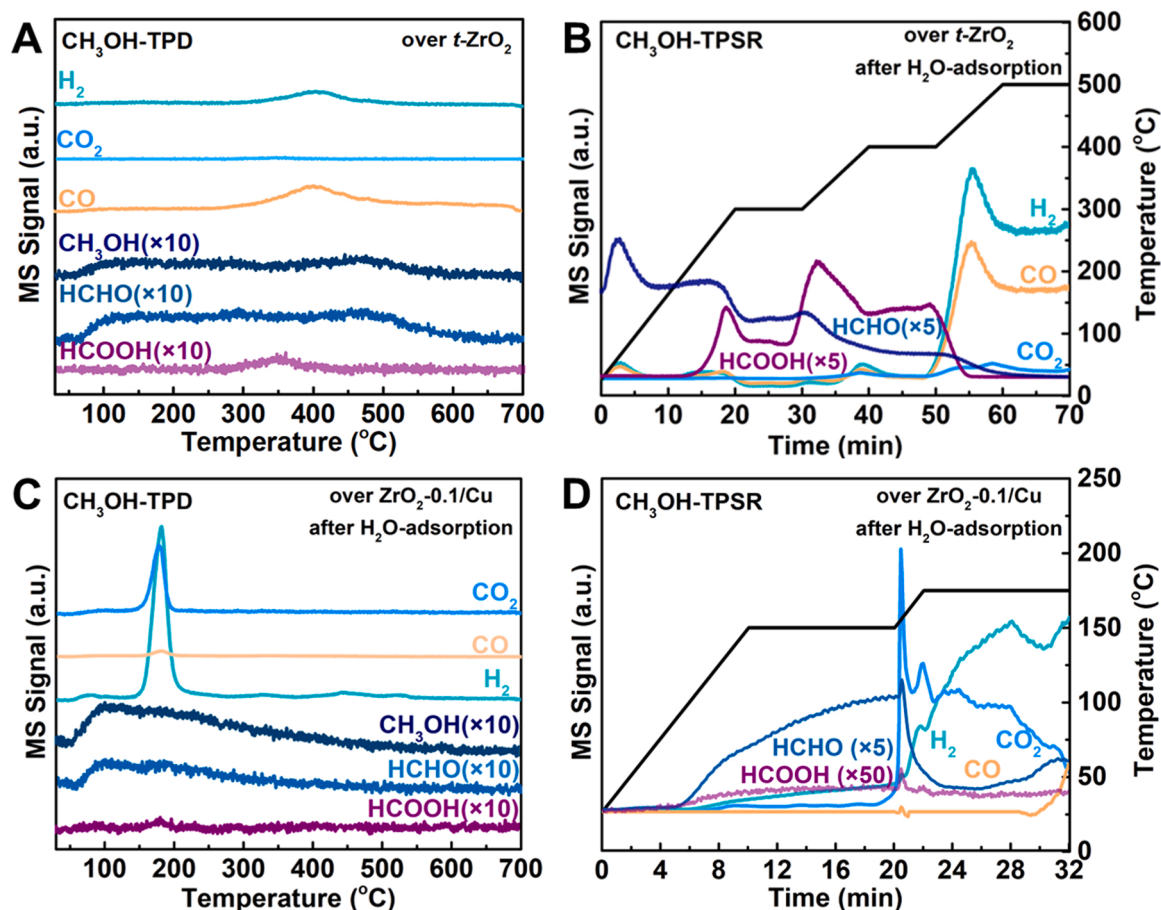

Fig. 5. (A, C) CH_3OH-TPD and (B, D) CH_3OH-TPSR profiles. Samples: in (A), neat t-ZrO_2; in (B), t-ZrO_2 after H_2O-adsorption at 200 °C; in (C) and (D), ZrO_2-0.1/Cu after H_2O-adsorption at 200 °C.

special synergistic catalysis between Cu^+/Cu sites and Zr-OH groups at the ZrO_2-Cu interface. To check this idea, the CH_3OH-TPD was performed on our representative ZrO_2-0.1/Cu catalyst, which was subject to H_2O-treatment at 200 °C in advance to form Cu^0/Cu^+ dual sites and grow Zr-OH on catalyst surface. In the profiles shown in Fig. 5C, a very weak and broad CH_3OH desorption peak with the maxima at 100 °C was detected from 50 to 450 °C; trace HCHO was formed while showing a temperature dependent evolution quite similar to that for the CH_3OH desorption. Most notably, very strong and narrow peaks of CO_2 and H_2 were detected with the peak temperature of 175 °C in association with the appearance of a pretty weak peak of HCOOH as well as a quite small CO peak.

In Fig. 5D, CH_3OH-TPSR profiles were recorded on such ZrO_2-0.1/Cu catalyst after H_2O-treatment at 200 °C. Clearly, detectable HCHO started to be formed at 100 °C while gradually increasing with rising temperature up to 150 °C, whereas the formation of $HCOOH/H_2/CO_2$ was detected only in trace amount even at 150 °C. Interestingly, when temperature was increased to 152 °C, the formation of CO_2 and H_2 suddenly boosts in association of detectable formation of HCOOH while HCHO shows a steep drop. Note that the trigger temperature of 152 °C for CO_2/H_2 formation is identical to the start temperature (153 °C) of the CO_2/H_2 peak observed in CH_3OH-TPD profile (Fig. 5C). Moreover, the formation of CO_2 and H_2 could be maintained at high level for several minutes even at 175 °C, undoubtedly due to the abundant Zr-OH groups (supplying -OH for reaction with HCHO to form CO_2/H_2). Indeed, along with prolonging time on stream, the CO_2 formation slid to a rapid decline trend, and meanwhile, the HCHO formation was detected again and improved while CO was formed from $HCHO/CH_3OH$ decomposition.

On the basis of the findings from Figs. 4 and 5, we believed that: (1) the t-ZrO_2 surface enriched with -OH groups is active for dissociative adsorption of CH_3OH to form HCHO and subsequently HCOOH, but is almost inert for further HCOOH decomposition to $CO/CO_2/H_2$ even at 400 °C (Fig. 5B); (2) the Cu^+/Cu sites on Cu substrate are also active for dissociative adsorption of CH_3OH to form HCHO and particularly get adsorbed HCHO efficiently reacting with surface OH groups to form CO_2/H_2 via HCOOH intermediates at around 175 °C (Fig. 4D); however, such advantage of Cu^+/Cu sites is covered up by the inadequate capacity for activating H_2O on Cu surface; (3) interestingly, when coupling both of them in our inverse ZrO_2/Cu catalyst, special synergistic catalysis between them is induced at ZrO_2-Cu interface (Fig. 5C, D).

3.4.4. Why interfacial -OH?

We also give an expression in the synergistic catalysis induced at the inverse ZrO_2-Cu interface: t-ZrO_2 nano-fragments offer abundant Zr-OH

groups next to Cu^+/Cu sites, thereby substantially boosting the reaction of adsorbed HCHO (from CH_3OH) on Cu^+/Cu sites with Zr-OH groups to form CO_2/H_2 with ultra-high selectivity via HCOOH intermediates. To prove this speculation more convincingly, the CH_3OH-pulse experiments were further implemented on the ZrO_2-0.1/Cu after H_2O-treatment at 200 °C, with profiles displayed in Fig. 6A. Along with CH_3OH-pulse going, the MS signal of CO_2 gradually weakened but CO signal gradually grew up as well as HCHO, due to the gradual consumption of -OH groups. This catalyst after CH_3OH-pulse test was probed by XPS in Zr 3d region, showing that the Zr-OH amount on catalyst surface is indeed reduced (Fig. 6B). Moreover, after -OH groups were supplemented by pulsing H_2O to the (-OH)-deficient catalyst surface, as expected, the overwhelming formation of CO_2 over CO was detected again (Fig. 6A). No doubt, the above results confirmed the essential role of Zr-OH as a supplier of reactive -OH in the synergistic catalysis induced at inverse ZrO_2-Cu interface.

The free -OH groups at pure t-ZrO_2 surface [45] proved to be almost inert for further decomposition of $CH_3OH/HCHO/HCOOH$ to form $CO/CO_2/H_2$ even at 400 °C (Fig. 5B), in turn indicating that the interfacial Zr-OH groups would be quite different with that free -OH on pure t-ZrO_2. As shown in the H_2O-TPD profile of the H_2O-adsorbed ZrO_2-0.1/Cu catalyst, four H_2O-desorption peaks were detected (Fig. S7C): besides the twos below 300 °C for the physically adsorbed H_2O and the one for the recombination of free -OH peaking at 500 °C, the moderate one centered at 340 °C appeared, which is ascribable to the interfacial -OH. In sharp contrast, the desorption of free -OH on pure t-ZrO_2 surface must be around 500 °C (Fig. S7A) [45,46]. It is rational to infer that the interfacial -OH at ZrO_2-Cu interface became more reactive than the free -OH on pure t-ZrO_2 surface, mostly due to the strong interaction with Cu^+/Cu sites at ZrO_2-Cu interface. In consequence, the MSR reaction is modulated by the $ZrO(OH)$-(Cu^+/Cu) complex sites toward hydrogen production with ultralow or even no CO formation, because of the boosted surface reaction of adsorbed HCHO (from CH_3OH) on Cu^+/Cu sites with Zr-OH groups to form CO_2/H_2 with ultra-high selectivity via HCOOH intermediates (see the theoretical calculations in posterior Section). What's more, the RWGS reaction was studied over the ZrO_2-0.1/Cu catalyst by TPSR-MS, using the CO_2/H_2 (1/3, mol/mol) feed. The TPSR-MS profiles in Fig. S8 showed that the RWGS reaction was hard to be catalyzed on the ZrO_2-0.1/Cu below 200 °C. Therefore, besides the synergistic effect at ZrO_2-Cu interface that suppressed the direct decomposition of methanol, we believe that the inertness of our ZrO_2-x/Cu catalysts for the RWGS reaction below 200 °C is another important contribution to the CO-free H_2 production via the MSR reaction.
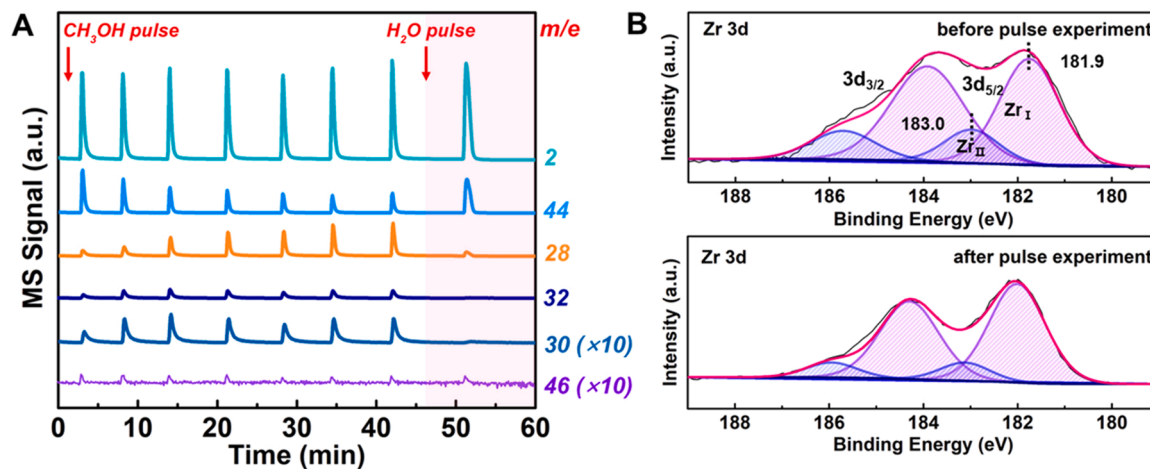

Fig. 6. Pulse tests and XPS spectra over ZrO_2-0.1/Cu. (A) CH_3OH/H_2O-pulse tests over ZrO_2-0.1/Cu at 200 °C and atmospheric pressure with each injection of CH_3OH or H_2O of 1 μL. (B) XPS spectra of Zr 3d for ZrO_2-0.1/Cu before (upper) and after (lower) the CH_3OH-pulse tests.

3.5. Theoretical calculations and reaction pathway

To gain further insight into the chemical and structural origin of such special ZrO_2-Cu interface catalysis in the MSR reaction at molecular level, the model of inverse Zr_3O_6/Cu(111) catalyst was built to simulate the real t-ZrO_2/Cu catalyst, which is depicted in Fig. 7A. On the basis of this model, the charge distribution was calculated, showing that there is no apparent electron transfer from Cu to t-ZrO_2 after geometry optimization. Nevertheless, the Cu species at the interface is partially electron-deficient with a mild charge transfer of 0.02 |e|. The above results confirm the existence of the interaction between Cu substrate and t-ZrO_2 cluster at interface [46]. What to be noted is that, regardless of the $Cu^{\delta+}$ species originated from Cu-ZrO_2 interaction or Cu^+ species formed by H_2O-oxidation in real MSR process, both of them promote the adsorption and activation of CH_3OH. Therefore, $Cu^{\delta+}$ species rather than Cu_2O are adopted in the model in order to simplify the calculations, and therefore the interfacial structure of Zr_3O_6/Cu(111) is referred as to

$Cu^{\delta+}$-O-Zr.

These steps, including CH_3OH dissociation to HCHO and H_2 on Cu (111), H_2O dissociation to -OH on t-ZrO_2, and HCOOH decomposition to CO_2/H_2 on Cu(111), have been extensively studied [37,47,48]. Herein, we aim to calculate the step of HCHO* reacting with OH* to HCOOH* at the Zr_3O_6-Cu(111) interface for showing the superiority of interfacial OH* species. The adsorption of OH* at interfacial and top sites were calculated with their adsorption energies of −1.53 eV (at interfacial Zr^1 site) and −1.31 eV (at top Zr^3 site) (Fig. 7B); the lower energy at Zr^1 site indicates a more stable Zr^1-OH configuration at interface. Moreover, the Zr-O^w bond length was also calculated and showed a longer length of 1.96 Å for $Zr^3O_xH_y$/Cu but a shorter one of 1.89 Å for $Zr^1O_xH_y$/Cu, which indicated the preferential formation of Zr^1-OH. Hence, the reaction of Zr^1-OH with HCHO* to CH_2OOH* was then calculated. The crucial intermediate of HCHO* could be stably adsorbed at $Cu^{\delta+}$ site with an energy of −0.62 eV (Fig. 7C). The Zr^1-OH (i.e., OH* at interfacial Zr^1 site) attacked the as-adsorbed HCHO* to form CH_2OOH* with
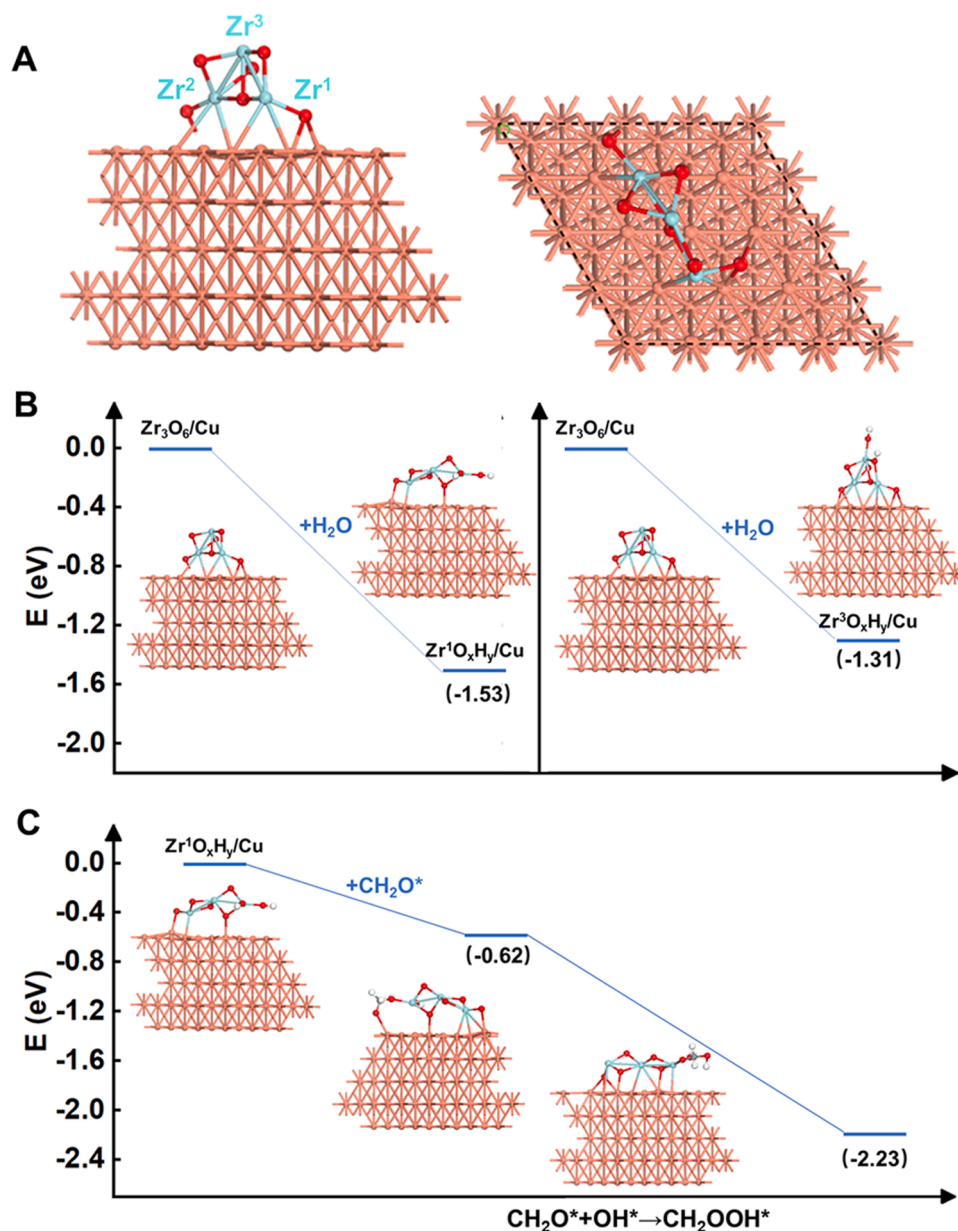

Fig. 7. Configuration and adsorption free energies of H_2O and CH_2O on Zr_3O_6/Cu(111). (A) Schematic views of optimized Zr_3O_6/Cu(111) model. (B) Optimized structures and adsorption energies (values in the bracket) of OH* adsorbed on the Zr^1 (left) and Zr^3 (right) sites of Zr_3O_6/Cu(111). (C) Energy profiles of CH_2O*-adsorption and CH_2O*-OH* combination on $Zr^1O_xH_y$/Cu(111). The Zr, Cu, C, H, and O atoms are given in cyan, orange, gray, white, and red, respectively.

a reaction energy of −1.61 eV (Fig. 7C), and such negative value suggested that this step proceeded feasibly at the ZrO_2-Cu interface. For the subsequent transformation of CH_2OOH^*, Lin et al. [48] explored the possible pathway on Cu(111) by density functional theory calculations, showing that CH_2OOH^* was preferentially to be converted into formate (HCOO*) than carboxyl (COOH*), and the HCOO* could be feasibly decomposed into CO_2 eventually.

4. Conclusions

We present an inverse ZrO_2/Cu catalyst system consisting of highly-dispersed t-ZrO_2 nano-fragments (3–4 nm) on Cu substrate (~20 nm particles), which can long-termly catalyze the MSR reaction to produce CO-free hydrogen with a high productivity of 190 $mmol_{H2}\ g_{cat}^{-1}\ h^{-1}$ at 200 °C. It is experimentally and theoretically unveiled that the outstanding MSR performance of our inverse catalyst is tightly linked with the $ZrO(OH)$-(Cu^+/Cu) complex sites built up at ZrO_2-Cu interface as well as crucial intermediates formed thereon. Specifically, the electron-deficient $Cu^{\delta+}$ sites are formed at interface to offer the $Cu^{\delta+}$-Cu^0 sites (referred as to Cu^+/Cu sites), which can effectively dissociate CH_3OH via Cu^0 abstracting H atoms and $Cu^{\delta+}$ adsorbing HCHO. The highly-dispersed t-ZrO_2 is responsible for H_2O-dissociation to offer abundant interfacial -OH neat to the Cu^+/Cu sites. Subsequently, the as-formed HCHO reacts with -OH to form HCOOH, followed by HCOOH decomposition into CO_2 and H_2. Obviously, the $ZrO(OH)$-(Cu^+/Cu) complex sites formed in real reaction stream paves an irreplaceable way to make HCHO and -OH accessible to each other to form HCOOH thereby avoiding the desorption and/or dehydrogenation of HCHO to form CO in essence.

Several points should be particularly noted for the ZrO_2/Cu catalyst. The first is about the reactivity of -OH species: the sole t-ZrO_2 can supply abundant -OH but shows poor reactivity, whereas the interfacial -OH can be modulated by the Cu-ZrO_2 interactions to be endowed with greatly meliorated reactivity, opening the channel for combination of HCHO and -OH to form HCOOH. The second, given that some HCHO is desorbed but with very little HCOOH-desorption during the TPSR of CH_3OH with adsorbed -OH groups on our ZrO_2/Cu catalyst, it is rational to infer that the HCHO-to-HCOOH step will overcome higher barrier than that of HCOOH-to-CO_2/H_2, suggesting that HCHO reacting with interfacial -OH to HCOOH represents the most crucial step at the $ZrO(OH)$-(Cu^+/Cu) complex sites. The third, the $ZrO(OH)$-(Cu^+/Cu) complex sites exhibit a good stability, which is linked to the efficient and continuous hydroxylation to form Zr-OH in actual reaction stream. In short, the findings of this work are highly instrumental to rationally tailor more-advanced catalyst and are essential for reactor and process design.

CRediT authorship contribution statement

Xinyi Xu: Writing – original draft, Investigation, Data curation, Formal analysis, Methodology. **Guofeng Zhao**: Supervision, Conceptualization, Writing – original draft, Data curation, Validation, Funding acquisition. **Tian Lan**: DFT calculations, Writing – original draft. **Qiang Nie**: Formal analysis. **Fengyang Jiang**: Formal analysis. **Yong Lu**: Supervision, Conceptualization, Project administration, Funding acquisition, Writing – review & editing. All authors discussed and commented on the manuscript.

Declaration of Competing Interest

The authors declare that they have no known competing financial interests or personal relationships that could have appeared to influence the work reported in this paper.

Data Availability

No data was used for the research described in the article.

Appendix A. Supporting information

Supplementary data associated with this article can be found in the online version at doi:10.1016/j.apcatb.2023.122839.

References

[1] M. Jacobson, W. Colella, D. Golden, Cleaning the air and improving health with hydrogen fuel-cell vehicles, Science 308 (2005) 1901–1905, https://doi.org/10.1126/science.1109157.

[2] K. Yu, W. Tong, A. West, K. Cheung, T. Li, G. Smith, Y. Guo, S. Tsang, Non-syngas direct steam reforming of methanol to hydrogen and carbon dioxide at low temperature, Nat. Commun. 3 (2012) 1230, https://doi.org/10.1038/ncomms2242.

[3] L. Lin, W. Zhou, R. Gao, S. Yao, X. Zhang, W. Xu, S. Zheng, Q. Yu, Y. Li, C. Shi, X. Wen, D. Ma, Low-temperature hydrogen production from water and methanol using Pt/alpha-MoC catalysts, Nature 544 (2017) 80–83, https://doi.org/10.1038/nature21672.

[4] C. Rameshan, W. Stadlmayr, C. Weilachm, S. Penner, H. Lorenz, M. Hävecker, R. Blume, T. Rocha, D. Teschner, A. Knop-Gericke, R. Schlögl, N. Memmel, D. Zemlyanov, G. Rupprechter, B. Klötzer, Subsurface-controlled CO_2 selectivity of PdZn near-surface alloys in H_2 generation by methanol steam reforming, Angew. Chem. Int. Ed. 49 (2010) 3224–3227, https://doi.org/10.1002/anie.200905815.

[5] X. He, Y. Wang, X. Zhang, M. Dong, G. Wang, B. Zhang, Y. Niu, S. Yao, X. He, H. Liu, Controllable in situ surface restructuring of Cu catalysts and remarkable enhancement of their catalytic activity, ACS Catal. 9 (2019) 2213–2221, https://doi.org/10.1021/acscatal.8b04812.

[6] J. Shen, C. Song, Influence of preparation method on performance of Cu/Zn-based catalysts for low-temperature steam reforming and oxidative steam reforming of methanol for H_2 production for fuel cells, Catal. Today 77 (2002) 89–98, https://doi.org/10.1016/S0920-5861(02)00235-3.

[7] L. Arroyo-Ramírez, C. Chen, M. Cargnello, C. Murray, P. Fornasiero, R. Gorte, Supported platinum-zinc oxide core-shell nanoparticle catalysts for methanol steam reforming, J. Mater. Chem. A 2 (2014) 19509–19514, https://doi.org/10.1039/C4TA04790G.

[8] F. Cai, J. Ibrahim, Y. Fu, W. Kong, J. Zhang, Y. Sun, Low-temperature hydrogen production from methanol steam reforming on Zn-modified Pt/MoC catalysts, Appl. Catal. B Environ. 264 (2020), 118500, https://doi.org/10.1016/j.apcatb.2019.118500.

[9] J. Lu, X. Li, S. He, C. Han, G. Wan, Y. Lei, R. Chen, P. Liu, K. Chen, L. Zhang, Y. Luo, Hydrogen production via methanol steam reforming over bi-based catalysts: Influences of Lanthanum (La) addition and supports, Int. J. Hydrog. Energ. 42 (2017) 3647–3657, https://doi.org/10.1016/j.ijhydene.2016.08.165.

[10] D. Li, F. Xu, X. Tang, S. Dai, T. Pu, X. Liu, P. Tian, F. Xuan, Z. Xu, I. Wachs, M. Zhu, Induced activation of the commercial Cu/ZnO/Al_2O_3 catalyst for the steam reforming of methanol, Nat. Catal. 5 (2022) 99–108, https://doi.org/10.1038/s41929-021-00729-4.

[11] J. Papavasiliou, G. Avgouropoulos, T. Ioannides, Effect of dopants on the performance of CuO-CeO_2 catalysts in methanol steam reforming, Appl. Catal. B Environ. 69 (2007) 226–234, https://doi.org/10.1016/j.apcatb.2006.07.007.

[12] B. Lindström, J. Agrell, L. Pettersson, Combined methanol reforming for hydrogen generation over monolithic catalysts, Chem. Eng. J. 93 (2003) 91–101, https://doi.org/10.1016/S1385-8947(02)00112-2.

[13] J. Papavasiliou, G. Avgouropoulos, T. Ioannides, Combined steam reforming of methanol over Cu-Mn spinel oxide catalysts, J. Catal. 251 (2007) 7–20, https://doi.org/10.1016/j.jcat.2007.07.025.

[14] I. Ritzkopf, S. Vukojević, C. Weidenthaler, J. Grunwaldt, F. Schüth, Decreased CO production in methanol steam reforming over Cu/ZrO_2 catalysts prepared by the microemulsion technique, Appl. Catal. A Gen. 302 (2006) 215–223, https://doi.org/10.1016/j.apcata.2006.01.014.

[15] K. Ploner, M. Watschinger, P. Nezhad, T. Götsch, L. Schlicker, E. Köck, A. Gurlo, A. Gili, A. Doran, L. Zhang, N. Köwitsch, M. Armbrüster, S. Vanicek, W. Wallisch, C. Thurner, B. Klötzer, S. Penner, Mechanistic insights into the catalytic methanol

steam reforming performance of Cu/ZrO$_2$ catalysts by in situ and operando studies, J. Catal. 391 (2020) 497–512, https://doi.org/10.1016/j.jcat.2020.09.018.

[16] X. Zhang, P. Shi, J. Zhao, M. Zhao, C. Liu, Production of hydrogen for fuel cells by steam reforming of methanol on Cu/ZrO$_2$/Al$_2$O$_3$ catalysts, Fuel Process. Technol. 83 (2003) 183–192, https://doi.org/10.1016/S0378-3820(03)00066-3.

[17] P. Finger, T. Osmari, M. Costa, J. Bueno, J. Gallo, The role of the interface between Cu and metal oxides in the ethanol dehydrogenation, Appl. Catal. A Gen. 589 (2020), 117236, https://doi.org/10.1016/j.apcata.2019.117236.

[18] N. Köwitsch, L. Thoni, B. Klemmed, A. Benad, P. Paciok, M. Heggen, I. Köwitsch, M. Mehring, A. Eychmüller, M. Armbrüster, Proving a paradigm in methanol steam reforming: catalytically highly selective In$_x$Pd$_y$/In$_2$O$_3$ interfaces, ACS Catal. 11 (2020) 304–312, https://doi.org/10.1021/acscatal.0c04073.

[19] M. Shen, G. Zhao, Q. Nie, C. Meng, W. Sun, J. Si, Y. Liu, Y. Lu, Ni-foam-structured Ni-Al$_2$O$_3$ ensemble as an efficient catalyst for gas-phase acetone hydrogenation to isopropanol, ACS Appl. Mater. Interfaces 13 (2021) 28334–28347, https://doi.org/10.1021/acsami.1c07084.

[20] K. Larmier, W. Liao, S. Tada, E. Lam, R. Verel, A. Bansode, A. Urakawa, A. Comas-Vives, C. Copéret, CO$_2$-to-methanol hydrogenation on zirconia-supported copper nanoparticles: reaction intermediates and the role of the metal-support interface, Angew. Chem. Int. Ed. 56 (2017) 2318–2323, https://doi.org/10.1002/anie.201610166.

[21] Z. Li, H. Hao, J. Lu, C. Wu, R. Gao, J. Li, C. Liu, W. Dong, Role of the Cu-ZrO$_2$ interface in the hydrogenation of levulinic acid to γ-valerolactone, J. Energ. Chem. 61 (2021) 446–458, https://doi.org/10.1016/j.jechem.2021.01.046.

[22] L. Mayr, B. Klötzer, D. Schmidmair, N. Köpfle, J. Bernardi, S. Schwarz, M. Armbrüster, S. Penner, Boosting hydrogen production from methanol and water by in situ activation of bimetallic Cu-Zr species, ChemCatChem 8 (2016) 1778–1781, https://doi.org/10.1002/cctc.201600361.

[23] R. Palomino, R. Gutiérrez, Z. Liu, S. Tenney, D. Grinter, E. Crumlin, I. Waluyo, P. Ramírez, J. Rodriguez, S. Senanayake, Inverse catalysts for CO oxidation: Enhanced oxide-metal interactions in MgO/Au(111), CeO$_2$/Au(111), and TiO$_2$/Au (111), ACS Sustain. Chem. Eng. 5 (2017) 10783–10791, https://doi.org/10.1021/acssuschemeng.7b02744.

[24] Y. Ma, J. Wang, K. Goodman, A. Head, X. Tong, D. Stacchiola, M. White, Reactivity of a zirconia-copper inverse catalyst for CO$_2$ hydrogenation, J. Phys. Chem. C. 124 (2020) 22158–22172, https://doi.org/10.1021/acs.jpcc.0c06624.

[25] G. Zhao, F. Yang, Z. Chen, Q. Liu, Y. Ji, Y. Zhang, Z. Niu, J. Mao, X. Bao, P. Hu, Y. Li, Metal/oxide interfacial effects on the selective oxidation of primary alcohols, Nat. Commun. 8 (2017) 14039, https://doi.org/10.1038/ncomms14039.

[26] L. Mayr, B. Klötzer, D. Zemlyanov, S. Penner, Steering of methanol reforming selectivity by zirconia-copper interaction, J. Catal. 321 (2015) 123–132, https://doi.org/10.1016/j.jcat.2014.10.012.

[27] G. Wu, D. Mao, G. Lu, Y. Cao, K. Fan, The role of the promoters in Cu based catalysts for methanol steam reforming, Catal. Lett. 130 (2009) 177–184, https://doi.org/10.1007/s10562-009-9847-8.

[28] T. Shodiya, O. Schmidt, W. Peng, N. Hotz, Novel nano-scale Au/α-Fe$_2$O$_3$ catalyst for the preferential oxidation of CO in biofuel reformate gas, J. Catal. 300 (2013) 63–69, https://doi.org/10.1016/j.jcat.2012.12.027.

[29] S. Zeng, Y. Wang, S. Ding, J.J. Sattler, E. Borodina, L. Zhang, B.M. Weckhuysen, H. Su, Active sites over CuO/CeO$_2$ and inverse CeO$_2$/CuO catalysts for preferential CO oxidation, J. Power Sources 256 (2014) 301–311, https://doi.org/10.1016/j.jpowsour.2014.01.098.

[30] C. Wu, L. Lin, J. Liu, J. Zhang, F. Zhang, T. Zhou, N. Rui, S. Yao, Y. Deng, F. Yang, W. Xu, J. Luo, Y. Zhao, B. Yan, X. Wen, J. Rodriguez, D. Ma, Inverse ZrO$_2$/Cu as a highly efficient methanol synthesis catalyst from CO$_2$ hydrogenation, Nat. Commun. 11 (2020) 5767, https://doi.org/10.1038/s41467-020-19634-8.

[31] T. Ghodselahi, M.A. Vesaghi, A. Shafiekhani, A. Baghizadeh, M. Lameii, XPS study of the Cu@Cu$_2$O core-shell nanoparticles, Appl. Surf. Sci. 255 (2008) 2730–2734, https://doi.org/10.1016/j.apsusc.2008.08.110.

[32] J. Zhang, J. Medlin, Catalyst design using an inverse strategy: from mechanistic studies on inverted model catalysts to applications of oxide-coated metal nanoparticles, Surf. Sci. Rep. 73 (2018) 117–152, https://doi.org/10.1016/j.surfrep.2018.06.002.

[33] M. Carreon, V. Guliants, Ordered meso- and macroporous binary and mixed metal oxides, Eur. J. Inorg. Chem. 1 (2005) 27–43, https://doi.org/10.1002/ejic.200400675.

[34] R. Wu, X. Zhao, Y. Liu, Atomic insights of Cu nanoparticles melting and sintering behavior in Cu-Cu direct bonding, Mater. Des. 197 (2021), 109240, https://doi.org/10.1016/j.matdes.2020.109240.

[35] M. Turco, G. Bagnasco, C. Cammarano, L. Micoli, M. Lenarda, E. Moretti, L. Storaro, A. Talon, The role of H2O and oxidized copper species in methanol steam reforming on a Cu/CeO2/Al2O3 catalyst prepared by one-pot sol-gel method, Appl. Catal. B Environ. 102 (2011) 387–394, https://doi.org/10.1016/j.apcatb.2010.12.010.

[36] A.G. Sato, D.P. Volanti, D.M. Meira, S. Damyanova, E. Longo, J.M.C. Bueno, Effect of the ZrO$_2$ phase on the structure and behavior of supported Cu catalysts for ethanol conversion, J. Catal. 307 (2013) 1–17, https://doi.org/10.1016/j.jcat.2013.06.022.

[37] W. Chen, S. Liu, M. Cao, C. Lu, Y. Xu, J. Li, Adsorption of methanol and methoxy on Cu(111) surface: a first-principles periodic density functional theory study, Chin. J. Chem. 24 (2006) 872–876, https://doi.org/10.1002/cjoc.200690166.

[38] B. Eren, C. Sole, J. Lacasa, D. Grinter, F. Venturini, G. Held, C. Esconjauregui, R. Weatherup, Identifying the catalyst chemical state and adsorbed species during methanol conversion on copper using ambient pressure X-ray spectroscopies, Phys. Chem. Chem. Phys. 22 (2020) 18806–18814, https://doi.org/10.1039/D0CP00347F.

[39] M. Turco, G. Bagnasco, C. Cammarano, P. Senese, U. Costantino, M. Sisani, Cu/ZnO/Al$_2$O$_3$ catalysts for oxidative steam reforming of methanol: the role of Cu and the dispersing oxide matrix, Appl. Catal. B Environ. 77 (2007) 46–57, https://doi.org/10.1016/j.apcatb.2007.07.006.

[40] S. Sá, H. Silva, L. Brandão, J. Sousa, A. Mendes, Catalysts for methanol steam reforming-a review, Appl. Catal. B Environ. 99 (2010) 43–57, https://doi.org/10.1016/j.apcatb.2010.06.015.

[41] A. Spitzer, A. Ritz, H. Lüth, The adsorption of H2O on Cu(100) surfaces, Surf. Sci. 152 (1985) 543–549, https://doi.org/10.1016/0039-6028(85)90186-4.

[42] K. Jung, A. Bell, The effects of synthesis and pretreatment conditions on the bulk structure and surface properties of zirconia, J. Mol. Catal. A: Chem. 163 (2000) 27–42, https://doi.org/10.1016/S1381-1169(00)00397-6.

[43] G. Wu, L. Wang, Y. Liu, Y. Cao, W. Dai, H. He, K. Fan, Implication of the role of oxygen anions and oxygen vacancies for methanol decomposition over zirconia supported copper catalysts, Appl. Surf. Sci. 253 (2006) 974–982, https://doi.org/10.1016/j.apsusc.2006.01.056.

[44] P. Zonetti, V. Bridi, G. Gonzalez, C. Moreira, O. Alves, R. Avillez, L. Appel, Isobutene from ethanol: describing the synergy between In$_2$O$_3$ and *m*-ZrO$_2$, ChemCatChem 11 (2019) 4011–4020, https://doi.org/10.1016/j.apsusc.2006.01.056.

[45] L. Mayr, X. Shi, N. Köpfle, B. Klötzer, D. Zemlyanov, S. Penner, Tuning of the copper-zirconia phase boundary for selectivity control of methanol conversion, J. Catal. 339 (2016) 111–122, https://doi.org/10.1016/j.jcat.2016.03.029.

[46] X. Tang, H. Zhang, C. Sun, X. Qiao, D. Ju, Adsorption mechanisms over ZrO$_2$-modified Cu(111) surface for X (CH$_3$OH, H$_2$O and CO): a DFT+U study, Surf. Sci. 716 (2022), 121976, https://doi.org/10.1016/j.susc.2021.121976.

[47] A. Hofmann, J. Sauer, Surface structure of hydroxylated and sulfated zirconia. A periodic density-functional study, J. Phys. Chem. B 108 (2004) 14652–14662, https://doi.org/10.1021/jp049220f.

[48] S. Lin, R. Johnson, G. Smith, D. Xie, H. Guo, Pathways for methanol steam reforming involving adsorbed formaldehyde and hydroxyl intermediates on Cu (111): density functional theory studies, Phys. Chem. Chem. Phys. 13 (2011) 9622–9631, https://doi.org/10.1039/C1CP20067D.